ROYAL SOCIETY OF CHEMISTRY

PAPER

Check for updates

Fabrication of LaFeO₃ and rGO-LaFeO₃ microspheres based gas sensors for detection of NO₂ and CO†

Neeru Sharma,[*a] Himmat Singh Kushwaha,[b] S. K. Sharma[a] and K. Sachdev [ID] [*ab]

In the present report, gas sensing devices based on $LaFeO_3$ and $rGO\text{-}LaFeO_3$ were fabricated by a photolithography technique. The X-ray diffraction, Raman spectra and FT-IR results confirm the formation of a perovskite phase and composite. XPS and TEM give the chemical compositions for both products. The higher roughness, greater surface area (62.1 m^2 g^{-1}), larger pore size (16.4 nm) and lower band gap (1.94 eV) of $rGO\text{-}LaFeO_3$ make it a suitable candidate to obtain high sensitivity. The gas sensing performance of the devices was investigated for various concentrations of NO_2 and CO gases at temperatures of 200 and 250 °C. It was observed that the $rGO\text{-}LaFeO_3$ based device exhibited a high relative response (183.4%) for a 3 ppm concentration of NO_2 at a 250 °C operating temperature. This higher response is attributed to the large surface area, greater surface roughness, and numerous active sites of $rGO\text{-}LaFeO_3$. The gas sensing properties investigated show that $rGO\text{-}LaFeO_3$ is an excellent candidate for an NO_2 sensor.

1. Introduction

Environmental concerns about health hazards due to the presence of toxic gases, such as CO, CO_2, NO_2, H_2, and O_3, and consequent safety regulations have necessitated the increased use of sensors in various settings from industrial sites to automobiles, the workplace and even homes. Among the various toxic gases, CO and NO_2 are the most hazardous air pollutants and are risky for humans, animals, and plants. According to the Occupational Safety and Health Administration (OSHA), the lowest tolerance limits for CO and NO_2 gases over a period of 8 h are ∼20 ppm and ∼5 ppm, respectively. Over-exposure to these gases could be a cause of disease and in extreme cases even loss of human life.[1] Therefore, the development of CO and NO_2 gas sensors which can detect minute concentrations of these toxic gases at low temperature is in high demand for environment protection. Nanomaterials have been shown to be promising materials for gas sensing because their high surface area provides more active sites for gas adsorption. Single and composite metal oxides, like SnO_2,[2] TiO_2,[3] ZnO,[4] In_2O_3,[5] WO_3,[6] Fe_2O_3,[7] ZnO–TiO_2,[8] and Fe doped ZnO,[9] are important materials for detecting small concentrations of harmful gases, but they

have associated problems, such as issues about long-term stability and high operating temperature. Graphene, a very famous carbonic material, shows excellent properties and the very high surface area which is necessary for the adsorption of minute concentrations of gases and shows high sensitivity towards the detection of dangerous gases. Graphene also displays a significant change in its electrical resistance after the adsorption of target gases, which further confirms graphene as a promising candidate for gas sensing.[10] Up to now, graphene-based materials synthesized by diverse methods have been used for the detection of gases at low operating temperatures, such as reduced graphene oxide (rGO) prepared by the thermal reduction of graphene oxide (GO)[11,12] and the chemical reduction of (GO),[13,14] and graphene obtained by chemical vapor deposition (CVD).[15,16] In particular, rGO has attracted much interest due to its great advantages of low cost and production in bulk quantities.[17] M. Gautam *et al.*[18] and Nanto *et al.*[19] have used graphene as a gas sensor and observed high sensitivity towards CH_4 and NH_3 gases. Also perovskite oxides (ABO_3) like $LaFeO_3$ and $SmFeO_3$ are well-known materials for gas sensing applications. In these materials the presence of a transition metal ion at a B-site and oxygen deficiencies play an important role in adsorption properties and catalytic behavior. $LaFeO_3$ exhibits outstanding chemical and physical properties for multifunctional applications like chemical sensors,[20] catalysts,[21] electrolytes,[22] fuel cells,[23] biosensors[24] and gas sensors.[25,26] A large number of rare earth sensing materials have been synthesized for the detection of CO and NO_x (toxic and combustible) gases.[26–29] The use of composites is a favorable scheme to

aDepartment of Physics, Malaviya National Institute of Technology, Jaipur 302017, India. E-mail: neerupathak93@gmail.com; ksachdev.phy@mnit.ac.in

bMaterials Research Centre, Malaviya National Institute of Technology, Jaipur 302017, India

† Electronic supplementary information (ESI) available. See DOI: 10.1039/c9ra09460a

improve sensor performance. Perovskite oxide and reduced graphene oxide are promising candidates as individual sensing materials: rGO is a highly sensitive gas sensing material whereas PO (ABO_3) provides a great ability to adjust its formulation by changing the elements on the A and/or B sites and doping. Hence a composite of rGO and $LaFeO_3$ would enhance the gas sensing performance, which is the objective of this work. The authors believe that this is the first work that has used rGO decorated $LaFeO_3$ for a gas sensing application. Gas sensing performance is generally influenced by the morphology and architecture of the materials, which are dependent on the synthesis route taken. There are several methods for the preparation of $LaFeO_3$ and rGO-$LaFeO_3$: *viz.* sol–gel,[30] co-precipitation,[31] ball milling[32] and hydrothermal[33] methods. Among these, the hydrothermal method is an effective tool for the controlled synthesis of perovskite oxide $LaFeO_3$ and rGO decorated $LaFeO_3$. Low-temperature growth, cost-effectiveness and an ability to control the size also make this method an efficient process.

We report the fabrication of gas sensors based on $LaFeO_3$ and its composite with rGO for the detection of CO and NO_2 gases. The gas sensing devices were fabricated on an IDE (interdigitated electrode) substrate through photolithography. The sensing materials were deposited on the IDE substrate by the drop cast method. A gas sensing study was undertaken for $LaFeO_3$ and rGO-$LaFeO_3$ devices under different concentrations of NO_2 and CO at temperatures of 200 and 250 °C. Synthesized samples of $LaFeO_3$ and rGO-$LaFeO_3$ were characterized by XRD, FTIR, TGA, Raman, XPS, FESEM, AFM, HRTEM, UV-Vis, and BET.
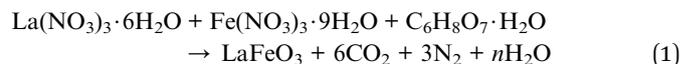
2. Experimental

2.1 Raw materials

Fine graphite powder (99.5%) and potassium permanganate (99%) were purchased from CDH. Sulfuric acid (98%) and hydrogen peroxide (30%) were purchased from RANKEM. Hydrogen chloride (12 N) was purchased from Merck. Lanthanum nitrate hexahydrate (99.9%), iron nitrate non-ahydrate (98+%) and citric acid (99+%) were purchased from Alfa Aesar.
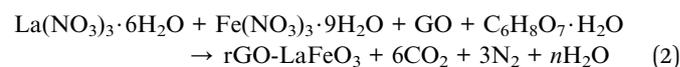
2.2 Synthesis of $LaFeO_3$

Lanthanum(III) nitrate hexahydrate ($La(NO_3)_3 \cdot 6H_2O$) and iron(III) nitrate nonahydrate ($Fe(NO_3)_3 \cdot 9H_2O$) were used as precursors and citric acid ($C_6H_8O_7 \cdot H_2O$) was used as a chelating agent to prepare $LaFeO_3$ microspheres using the hydrothermal method.[34] $La(NO_3)_3 \cdot 6H_2O$ (0.2 mol) and $Fe(NO_3)_3 \cdot 9H_2O$ (0.2 mol) were dissolved in 80 mL of DI water under magnetic stirring for 10 minutes. Subsequently, citric acid (0.4 mol) was added to the solution under continuous magnetic stirring for 10 minutes and the reaction mixture was poured into a 100 mL Teflon-lined stainless steel autoclave and kept at 160 °C for 6 h. After cooling down to room temperature (RT), precipitates were collected by centrifugation at 4000 rpm from the autoclave, and washed with DI water and ethanol. The collected precipitates were dried in air at 60 °C, followed by calcination at 800 °C for

4 h to obtain powdered $LaFeO_3$. The reaction between the above salts in the presence of citric acid is assumed to occur in the way shown in eqn (1).[34]

$$La(NO_3)_3 \cdot 6H_2O + Fe(NO_3)_3 \cdot 9H_2O + C_6H_8O_7 \cdot H_2O$$
$$\rightarrow LaFeO_3 + 6CO_2 + 3N_2 + nH_2O \quad (1)$$

2.3 Synthesis of rGO-$LaFeO_3$

$La(NO_3)_3 \cdot 6H_2O$ (0.2 mol) and $Fe(NO_3)_3 \cdot 9H_2O$ (0.2 mol) were dissolved in 80 mL of DI water under magnetic stirring for 10 minutes; then 200 mg of graphene oxide was added to the solution under ultrasonication at 50 °C for 1 h until the GO was well dispersed in the solution.[35] GO was prepared by Hummers' method.[36] An appropriate amount of citric acid (0.4 mol) was added to the solution under magnetic stirring for 30 minutes with the same follow-up as that for the preparation of $LaFeO_3$ to obtain rGO-$LaFeO_3$ powder. The reaction for the synthesis of the rGO-$LaFeO_3$ composite is assumed to occur as shown in eqn (2). The pathway for the synthesis of $LaFeO_3$ and its composite with rGO is shown in Fig. 1.

$$La(NO_3)_3 \cdot 6H_2O + Fe(NO_3)_3 \cdot 9H_2O + GO + C_6H_8O_7 \cdot H_2O$$
$$\rightarrow rGO\text{-}LaFeO_3 + 6CO_2 + 3N_2 + nH_2O \quad (2)$$

In this work, ethylene glycol (EG) was used as a solvent. For the preparation of the $LaFeO_3$/rGO-$LaFeO_3$ solution, 12 mg of $LaFeO_3$/rGO-$LaFeO_3$ were dissolved in 1 mL of EG. The solution was then sonicated at 50 °C for 2 hours to be used for film preparation, as shown in Fig. 2(a and b).

2.4 Fabrication of $LaFeO_3$/rGO-$LaFeO_3$–IDE based device

For CO and NO_2 detection, $LaFeO_3$ and rGO-$LaFeO_3$ thin films were deposited on an interdigitated electrode (IDE) substrate. To prepare the IDE substrate, an oxide layer ($SiO_2 \sim 200$ nm) was grown on a cleaned p-type Si wafer using a pyrogenic wet oxidation process. After that a thick layer of photo resist (AZ5214E PR) was spin coated on the SiO_2/p-Si substrate, followed by photolithography, sputtering of 10 nm Cr/120 nm Au and lifting off the photo-resist to produce a pattern of Au heating lines (125 nm thick) on the substrate. After the lift-off process AZ5214E PR was again spin coated above the Cr/Au film followed by photolithography for the gas sensing layer. $LaFeO_3$/rGO-$LaFeO_3$ solutions were then drop caste on the Si-IDE substrate after lifting off the photo resist and dried at 200 °C for 2 : 30 hours. The flow process for the fabrication of an IDE deposited $LaFeO_3$/rGO-$LaFeO_3$ gas sensor is shown in Fig. 2(c). The device size was 500×500 μm, with 100 fingers. The width of each finger was 5 μm with the same spacing between two fingers.

2.5 Characterizations studies

As-synthesized samples of $LaFeO_3$ and its composite with reduced graphene oxide (rGO-$LaFeO_3$) were characterized by X-ray diffraction (XRD; X-pert powder diffractometer with
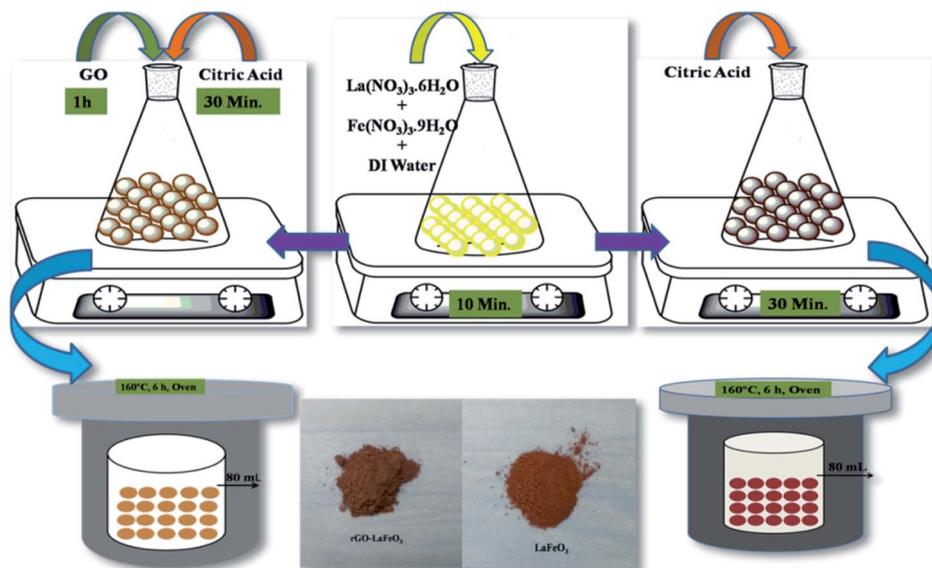
Fig. 1 Pathway for the formation of $LaFeO_3$ and $rGO-LaFeO_3$ microspheres.

copper rotating anode using incident beam of 1.54 Å wavelength), Fourier transform infrared spectroscopy (FTIR; PerkinElmer system in the KBr mode), Raman spectroscopy (STR 500 Confocal Micro Raman Spectrometer at 532 nm wavelength), thermo-gravimetric analysis (TGA; PerkinElmer STA 6000), a field emission scanning electron microscope (FESEM; 450 FEI, NOVA nano SEM), a transmission electron microscope (TEM-Tecnai G^2 XFLESH-6T130 with accelerating voltage 200 kV), an atomic force microscope (AFM using non-contact mode), a UV-Vis spectrometer (UV-Vis, Lambda 750,

PerkinElmer), and X-ray photoelectron spectroscopy (XPS, Omicron Nanotechnology, Oxford Instruments Germany). XPS wide scans and C 1s and O 1s spectra were recorded using AlK$_\alpha$ radiation ($h\nu = 1486.6$ eV). The pass energy for the C 1s and O 1s spectra was kept at 50 eV and 20 eV for full scans. Brunauer–Emmett–Teller (BET; Quantachrome instruments: NOVA touchLX1) was used to examine the surface area, and gas sensing measurements were recorded by Eurotherm 2404, Keithley-2450 at IISc Bangaluru.
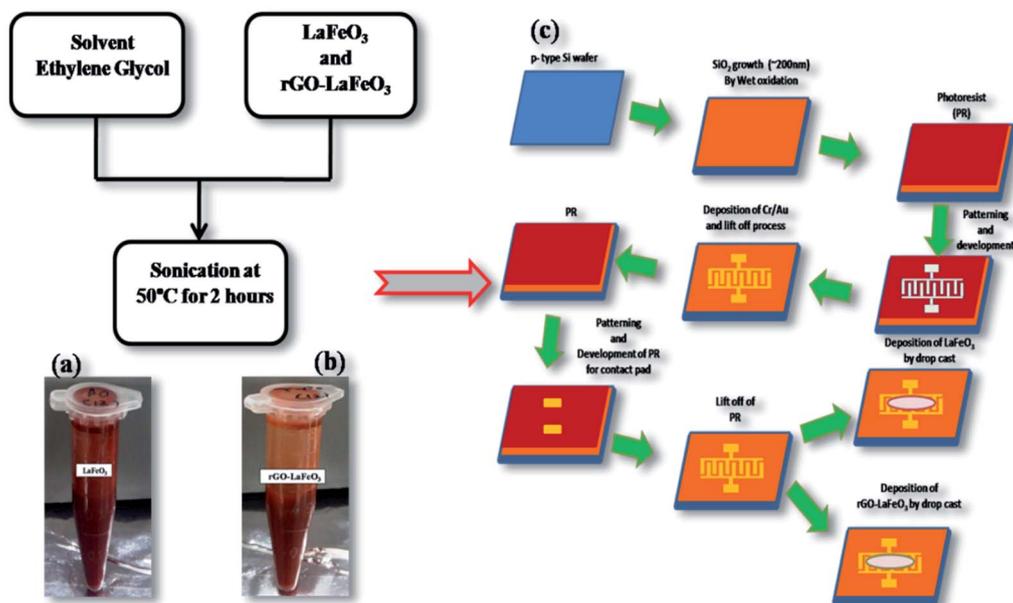

Fig. 2 Solution formation of $LaFeO_3$ (a) and $rGO-LaFeO_3$ (b) using solvent EG. Fabrication process of IDE deposited $LaFeO_3/rGO-LaFeO_3$ (c). Both samples are deposited by drop casting on an IDE pattern.

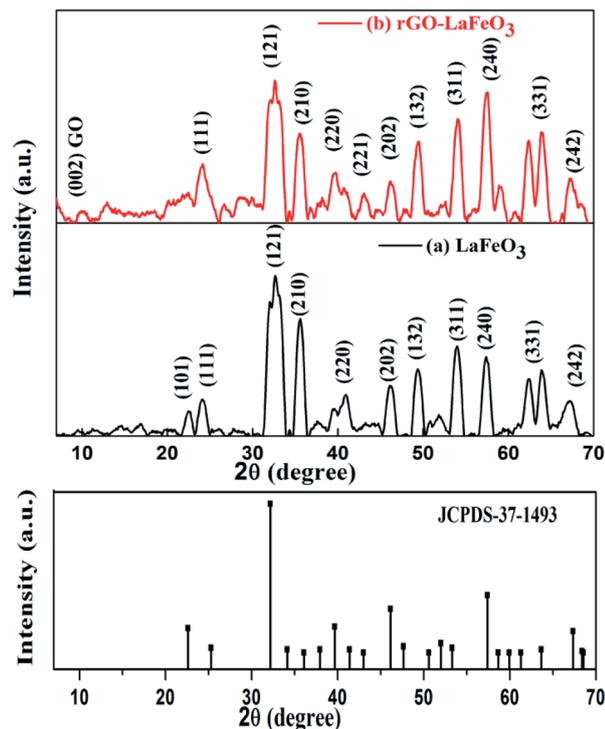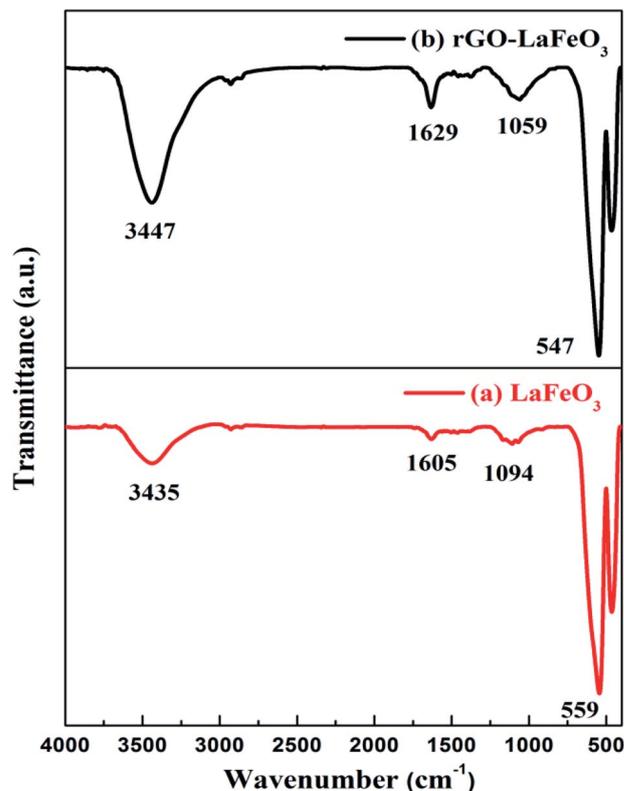**Fig. 3** XRD spectra for LaFeO$_3$ (a) and rGO-LaFeO$_3$ (b) with JCPDS-37-1493.

Fig. 4 FTIR spectra for LaFeO$_3$ (a) and rGO-LaFeO$_3$ (b).

3. Result and discussion

3.1 X-ray diffraction studies

The XRD patterns of LaFeO$_3$ and rGO-LaFeO$_3$ shown in Fig. 3(a) and (b) give information about the phases present and the crystallinity of the samples. Characteristic peaks of obtained LaFeO$_3$ microspheres were indexed using JCPDS-37-1493.[24,26,37] Strong and highly intense peaks indicate good crystallinity of synthesized LaFeO$_3$. No impurity peaks were observed in the XRD pattern. A d-spacing of LaFeO$_3$ microspheres corresponding to a highly intense plane (121) was found at 2.7 Å. These results suggest an orthorhombic structure for LaFeO$_3$ with lattice parameters $a = 5.565$ Å, $b = 7.839$ Å, and $c = 5.577$ Å.[37] The XRD pattern in Fig. 3(b) for the rGO-LaFeO$_3$ composite comprises peaks assigned to individual LaFeO$_3$, as shown in Fig. 3(a), belonging to the orthorhombic LaFeO$_3$ phase. A small peak at 10.02° was attributed to the (002) plane arising from the presence of rGO in the synthesized composite.[38] The d-spacing corresponding to the (121) plane of rGO-LaFeO$_3$ was observed at 2.6 Å. Background noise in XRD spectra may be due to instrumental error, and the splitting of the peaks can be removed after calcining the samples at higher temperature and for a longer duration.[37]

3.2 FT-IR studies

FT-IR spectra for LaFeO$_3$ and rGO-LaFeO$_3$ were recorded in a range of 400–4000 cm^{-1} wavenumbers to monitor the functional groups present in the materials and are given in

Fig. 4(a) and (b), respectively. For LaFeO$_3$, bands were observed at 559, 1094, 1605 and 3435 cm^{-1}. The band at 559 cm^{-1} is the characteristic band indicating the presence of Fe–O stretching.[39,40] This peak confirms the formation of a perovskite phase, and usually appears in the range of 500–700 cm^{-1}. Peaks at 1605 cm^{-1} and 3435 cm^{-1} are assigned to asymmetric stretching of the carboxyl group and hydroxyl group.[38] These peaks were shifted to 547, 1059, 1629 and 3447 cm^{-1}, when LaFeO$_3$ was decorated with rGO. The peak at 1629 cm^{-1} corresponding to the C═C/C–C stretching of the alkene or aromatic group confirms the sp^2 structure of rGO.[41] For further confirmation of perovskite formation and the presence of rGO in the composite, Raman spectroscopy was performed and is given in ESI (Fig. S1†). The thermal stability of the synthesized samples was studied by TGA and is given in ESI Fig. S2.†

3.3 Field emission scanning electron microscopy studies

The surface morphologies of LaFeO$_3$ and rGO-LaFeO$_3$ were observed using FESEM and the micrographs obtained are shown in Fig. 5(a) and (b), respectively. Fig. 5(a) shows the microsphere formation of LaFeO$_3$ with an average size of 1.45 μm. In Fig. 5(b) it can be observed that rGO decorated LaFeO$_3$ microspheres showed an average size of 1.57 μm. The layered structure of rGO between the microspheres of LaFeO$_3$ can clearly be seen in Fig. 5(b). In both samples of LaFeO$_3$ and rGO-LaFeO$_3$ microspheres are formed due to the coagulation of
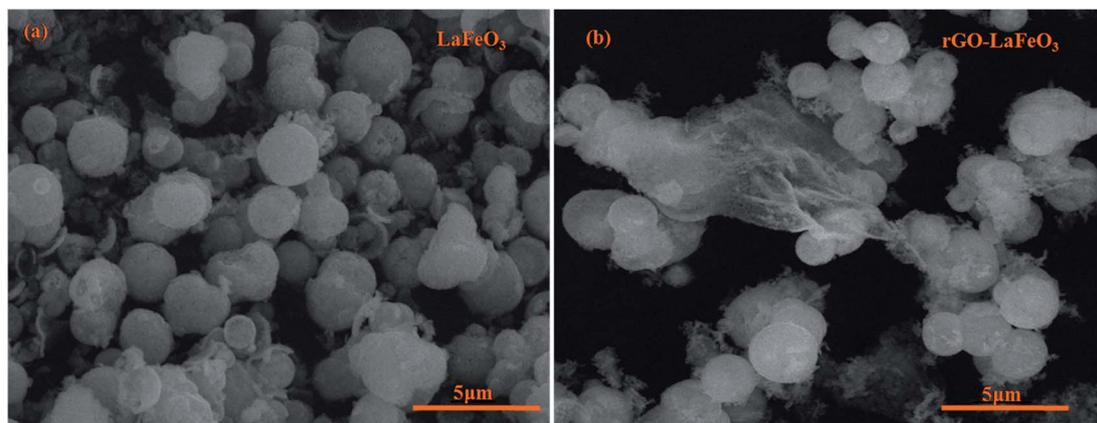
Fig. 5 FESEM images for LaFeO₃ (a) and rGO–LaFeO₃ (b).

a large number of nanoparticles. The TEM results, as shown in Fig. 6 and 7, provide more information about the microstructure.

3.4 High-resolution transmission electron microscopy studies

Fig. 6(a)–(c) show low and high magnification TEM images of synthesized LaFeO₃ microspheres. It was observed that the

prepared LaFeO₃ shows a sphere-like structure with high porosity. Fig. 6(b and c) confirm that porous microspheres are arranged in a network form with a large number of particles. The HRTEM image of a porous LaFeO₃ microsphere shown in Fig. 6(d) is indicative of the formation of interference fringes with a lattice perpendicular (*d*-spacing) of about 0.268 nm, in agreement with the plane (121) of LaFeO₃ observed from XRD. The selected area electron diffraction (SAED) pattern shown in
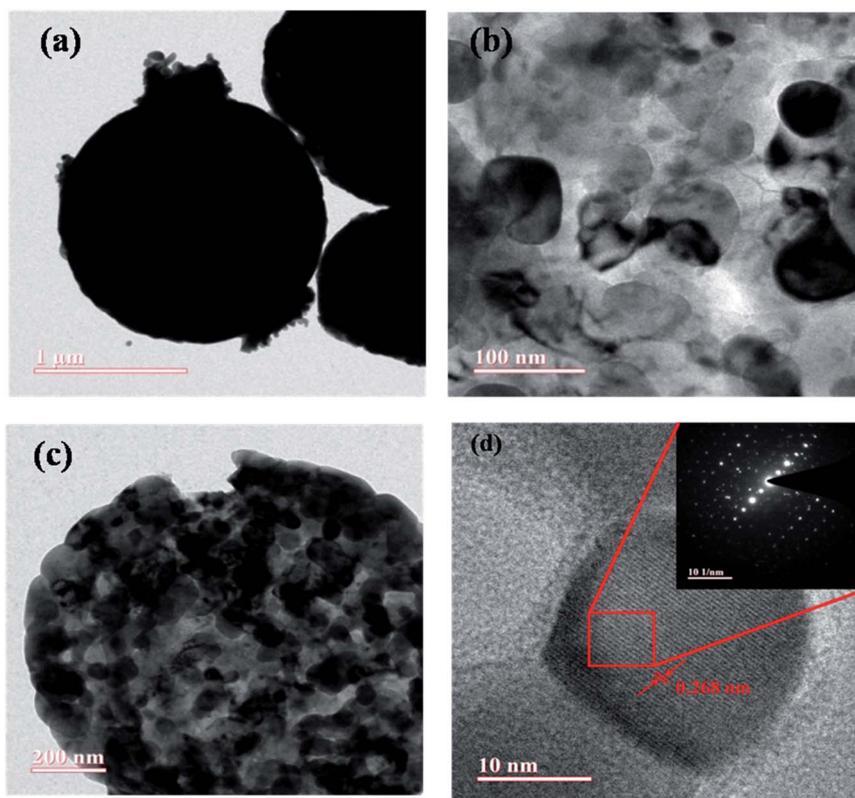

Fig. 6 Low (a) and high magnification (b and c) TEM images of porous LaFeO₃ microspheres, and the corresponding HRTEM image with labeled lattice spacing (inset: SAED pattern of LaFeO₃ microsphere) (d).
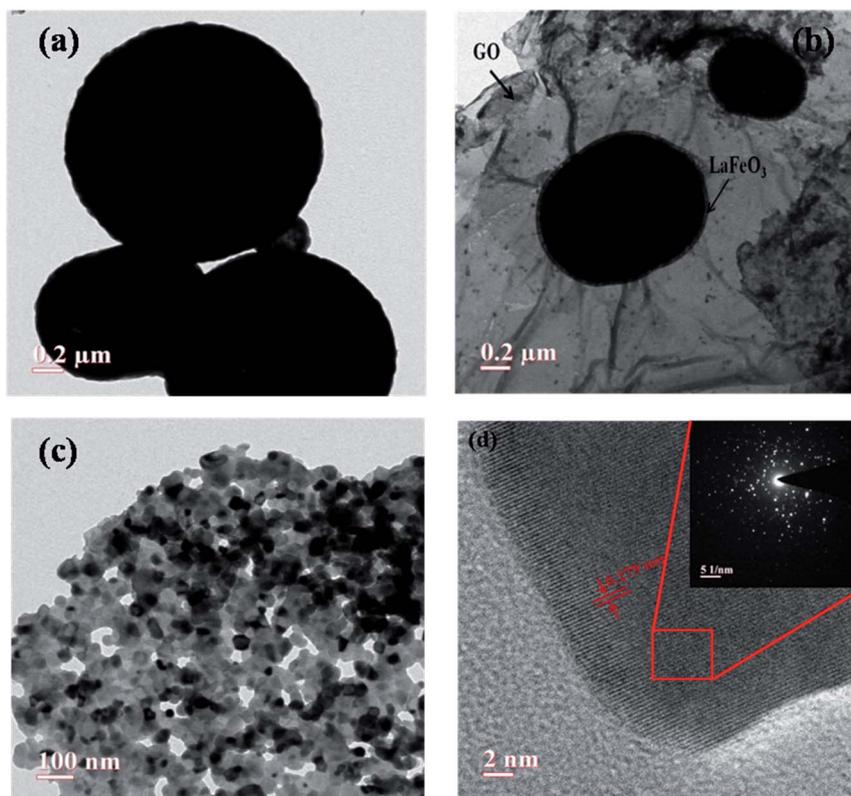
Fig. 7 (a and b) Low and (c) high magnification TEM image of porous rGO-LaFeO$_3$ microspheres, (d) the corresponding HRTEM image with labeled lattice spacing (inset: SAED pattern of rGO-LaFeO$_3$ microsphere).

the inset of Fig. 6(d) clearly indicates the polycrystalline nature of the prepared porous LaFeO$_3$ microspheres. The average diameter of a microsphere was found to be about 1.45 μm, as calculated by Image J software. This size of the microsphere coincides with that obtained from the FESEM study.

Low and high magnification TEM images of prepared rGO-LaFeO$_3$ composites are shown in Fig. 7(a)–(c), respectively. Fig. 7(a) and (b) show that porous microspheres of LaFeO$_3$ are decorated on the surface of the GO layer and the GO sheets show interconnections with the LaFeO$_3$ microspheres. From Fig. 7(c) it is clear that the LaFeO$_3$ microspheres are well distributed on the GO surface, which would be beneficial for making a significant surface area in the composite for sensing gases. The HRTEM image of the rGO-LaFeO$_3$ composite shown in Fig. 7(d) clearly indicates interference fringes with a d-spacing of about 0.279 nm and suggest the growth of LaFeO$_3$ microspheres on the GO surface. The d-spacing for the composite rGO-LaFeO$_3$ (0.279 nm) as compared to that for LaFeO$_3$ (0.268 nm) confirms that no structural change occurred in the composite. The corresponding SAED spectra shown in the inset of Fig. 7(d) show that the microspheres are randomly oriented in the composite. The size of the LaFeO$_3$ microspheres in the composite using Image J software was obtained as 1.57 μm. EDAX spectra and the percentages of the elements in the

synthesized samples are shown in ESI Tables S1 and S2,† respectively.

3.5 X-ray photoelectron spectroscopy studies

X-ray photoelectron spectroscopy (XPS) has proved to be a useful tool for identifying the valence states of La and Fe in the synthesized samples LaFeO$_3$ and rGO-LaFeO$_3$. Casa XPS software was used for peak fitting of La 3d, Fe 2p, C 1s and O 1s spectra with Shirley background correction. Fig. 8(a) shows wide range survey spectra for LaFeO$_3$ and rGO-LaFeO$_3$ and the observed characteristic peaks attributed to La, Fe, oxygen, and carbon. XPS spectra for LaFeO$_3$ shown in Fig. 8(b)–(d) correspond to La 3d, Fe 2p, and O 1s, respectively. From Fig. 8(b) it can be seen that La deconvoluted into four peaks; among them, peaks corresponding to binding energies (BE) of 833.6 eV and 850.4 eV are assigned to La 3d$_{5/2}$ and La 3d$_{3/2}$, respectively.[42–44] The other two peaks at binding energies of 837.6 eV and 854.4 eV are satellite peaks corresponding to La 3d$_{5/2}$ and La 3d$_{3/2}$, respectively.[44] This information about the core level of La indicates that La ions exhibit +3 oxidation states. The BE of the Fe 2p$_{3/2}$ signal has been found in the energy range 706.5–707.0 eV for metallic iron, 709.5–710.3 eV for Fe^{2+}, and 710.6–711.4 eV for Fe^{3+}.[45] In Fig. 8(c), the peaks at binding energies 709.5 eV and 712.8 eV are attributed to the spin–orbit of Fe 2p$_{3/2}$.[45] The binding energy at 725.1 eV is assigned to Fe 2p$_{1/2}$ for Fe^{3+}.[46] The other
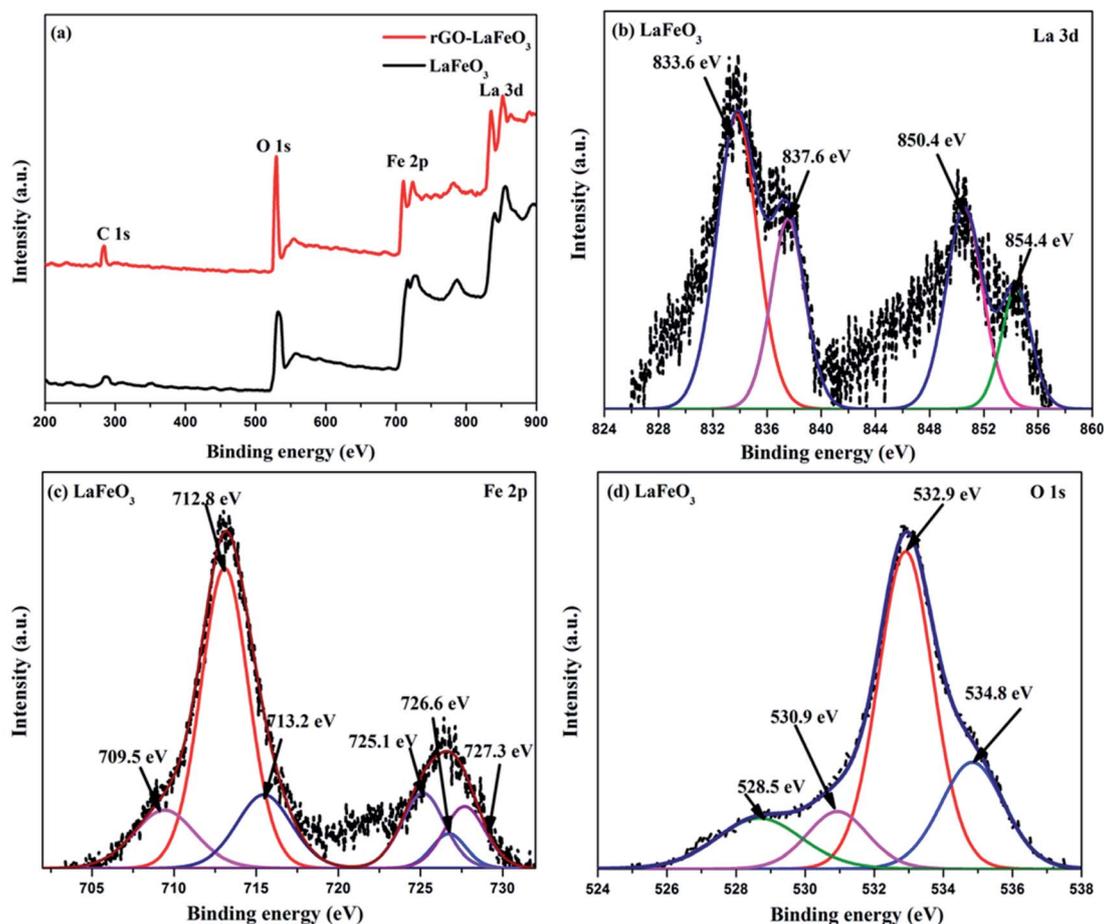
Fig. 8 Wide range survey spectra (a) of $LaFeO_3$ and rGO-$LaFeO_3$, XPS spectra of La 3d (b), Fe 2p (c), O 1s (d) for $LaFeO_3$.

two peaks at 726.6 eV and 727.3 eV may be due to the presence of some Fe^{4+} state of Fe $2p_{1/2}$, which is not seen in XRD.[43] Thus the results indicate that Fe contains mixed valence state of Fe^{3+} and Fe^{4+} in the main. This combination of valence states is rare and was observed by Phokha *et al.* in 2014.[43] The XPS peaks of oxygen spectra are deconvoluted into four peaks; among them the peak corresponding to a binding energy of 528.5 eV confirms the existence of crystal lattice oxygen (O_L) and the peak located at 530.9 eV binding energy confirms the presence of hydroxyl oxygen (O_H).[1] The core level of the La 3d region for the composite shown in Fig. 9(a) exhibits peak positions at 833.5 eV and 850.2 eV assigned as La $3d_{5/2}$ and La $3d_{3/2}$, respectively. This indicates that La ions have mainly an La^{3+} state. La 3d satellite peaks are assigned at 837.6 eV and 854.5 eV binding energies, respectively.[44] Fig. 9(b) for the core level region of Fe 2p for sample rGO-$LaFeO_3$ shows peaks located at 710.7 eV and 711.7 eV binding energies, corresponding to Fe $2p_{3/2}$. The peaks at BE 723.2 eV and 724.9 eV are attributed to Fe $2p_{1/2}$. This indicates that Fe ions in rGO-$LaFeO_3$ also have a mixed state of Fe^{3+} and Fe^{4+}.[43,45] In addition, the peak at 709.1 eV, corresponding to $Fe2p_{3/2}$, may be due to the presence of the Fe^{2+} state of Fe_2O_3.[45] A broad peak at 718.2 eV is a shake-up

satellite peak of Fe^{3+}.[45,47] For the O 1s spectra of rGO-$LaFeO_3$, similar peak positions at 528.4 eV for O_L and at 530.9 eV for O_H were observed.[24] The XPS spectrum of C ls shown in Fig. 9(d) deconvoluted into three peaks due to hydrocarbons and hydroxyls. The peak at 283.6 eV is associated with (C=C), 285.4 eV corresponds to (C–C/C–H) and 287.3 eV is associated with the hydroxyl group (C–OH).[48–50]

3.6 UV-visible spectroscopy

Fig. 10(a) shows the UV-Vis absorption spectra of $LaFeO_3$ and its composite with rGO in the wavelength range 200–1300 nm. It was observed from the spectra that both samples show a strong absorption in the ultraviolet (200–400 nm) and visible (400–800 nm) regions. The UV-Vis spectra allow us to calculate the direct band gap E_g by fitting the absorption data to the direct transition using Tauc's formula ($\alpha h\nu = A(h\nu - E_g)^{1/2}$, where α is the absorption coefficient, $h\nu$ is the photon energy, A is a constant, and E_g is the direct band gap) by plotting $(\alpha h\nu)^2$ *versus* $h\nu$, as shown in Fig. 10(b). The calculated band gaps are 1.94 eV for rGO-$LaFeO_3$ and 2.01 eV for $LaFeO_3$, indicating a slight narrowing of the band gap on the addition of rGO to $LaFeO_3$. This would be useful for the movement of electrons from the valence band to the conduction band for gas sensing.
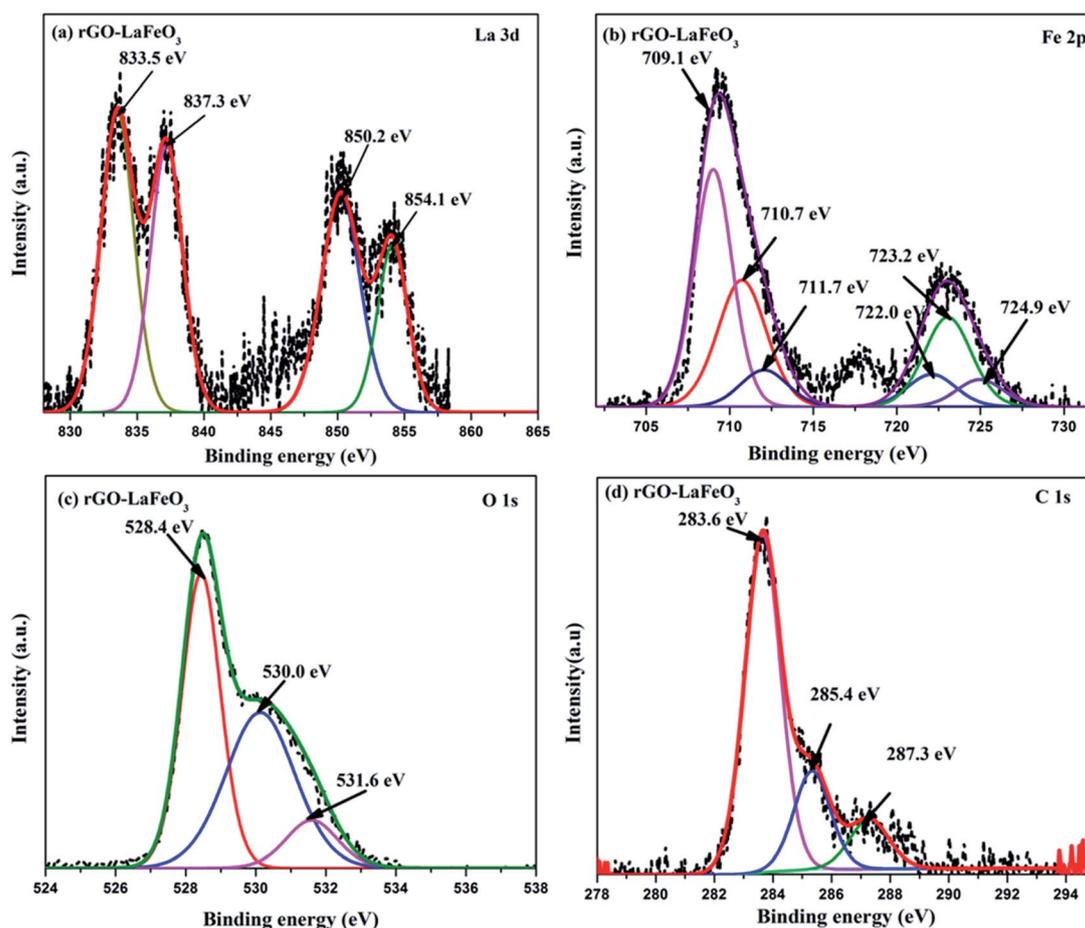
Fig. 9 XPS spectra of La 3d (a), Fe 2p (b), O 1s (c), and C 1s (d) for rGO-LaFeO$_3$.

3.7 Adsorption–desorption isotherm, surface area and pore size distribution

Fig. 11(a–c) display the adsorption–desorption curves (N$_2$) and the obtained surface areas of the synthesized samples. It can

clearly be seen that the isotherm changes from type II for LaFeO$_3$ (shown in the inset) to type III for rGO-LaFeO$_3$.[51] The pore size for LaFeO$_3$ comes out to be 1.85 nm, and increased to 16.4 nm for rGO-LaFeO$_3$.[52] Hence, according to the pore size
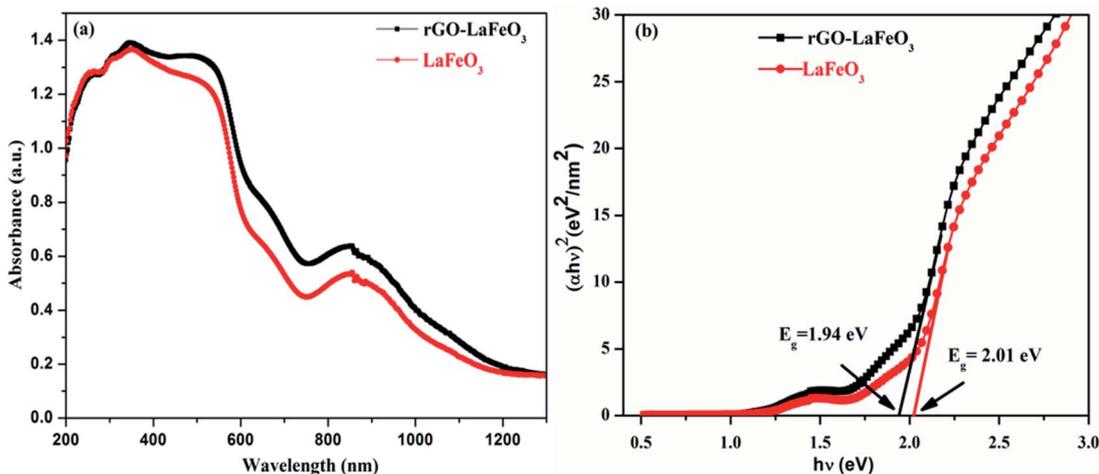

Fig. 10 Absorption spectra (a) and Tauc plot (b) of LaFeO$_3$ and rGO-LaFeO$_3$.
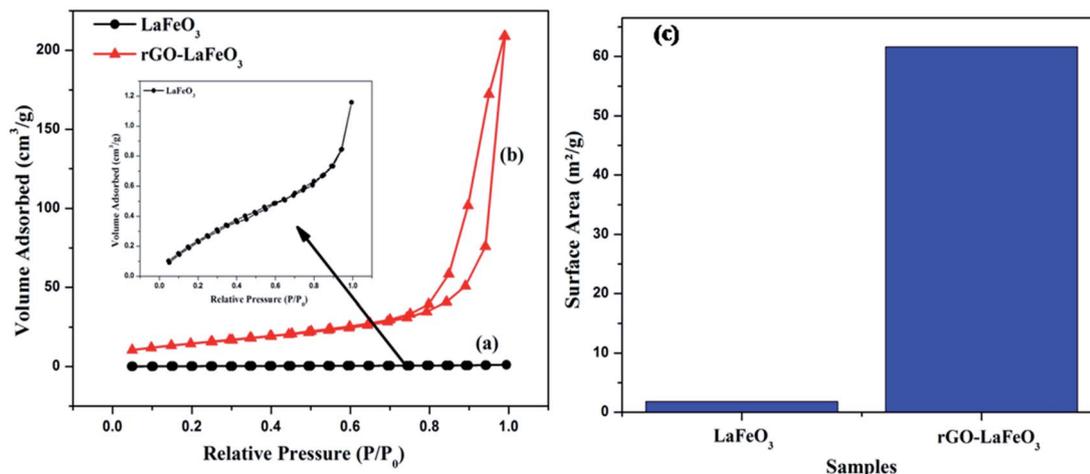
Fig. 11   N$_2$ adsorption–desorption isotherm spectra of (a) LaFeO$_3$, (b) rGO-LaFeO$_3$ and surface area of (c) LaFeO$_3$, rGO-LaFeO$_3$.

and type of isotherm, the samples can be categorized as having a micro porous and a mesoporous structure for LaFeO$_3$ and rGO-LaFeO$_3$, respectively. The surface area for composite rGO-LaFeO$_3$ is about forty times ∼62.1 m^2 g^{-1} (Fig. 11(c)) that of LaFeO$_3$ ∼1.41 m^2 g^{-1}. This many-fold increase in surface area is due to the addition of rGO to LaFeO$_3$, and is a useful property.

3.8   Gas sensing studies

It is evident from the studies carried out that LaFeO$_3$ and rGO-LaFeO$_3$ materials meet the criteria for realization of a gas sensor. These films were then employed for CO and NO$_2$ gas sensing by sourcing a voltage of 6 V and measurement of current/resistance through Cr/Au contact pads resting on an IDE deposited on the films by photolithography. A photograph of the fabricated gas sensor with Cr/Au contact is shown in Fig. 12. Compressed air was used as a carrier gas (N$_2$ + O$_2$ = 80% + 20%) to which 1–3 ppm CO and 1–5 ppm NO$_2$ were added from a second cylinder whilst maintaining a constant flow rate of 30 sccm. The gas sensing characteristics are

Fig. 12   Gas sensing device based on LaFeO$_3$ and rGO-LaFeO$_3$.

plotted as change in ratio defined as follows: as change in resistance for CO and NO$_2$ gases in opposite polarity. Here R_a and R_g are the resistance of the specimens in air and gas, respectively.

$$S(\%) = \frac{R_g - R_a}{R_a} \times 100 \text{ for CO exposure} \quad (3)$$

$$S(\%) = \frac{R_a - R_g}{R_g} \times 100 \text{ for NO}_2 \text{ exposure} \quad (4)$$

3.8.1   Carbon monoxide gas sensing. Fig. 13(a) and (b) show the plots of relative response(s) for LaFeO$_3$ and rGO-LaFeO$_3$ as a function of time. Both samples were tested in the presence of 5, 3 and 1 ppm CO gas at temperatures of 200 and 250 °C. However, LaFeO$_3$ does not show any response at 200 °C while a good response was found at 250 °C. For the p-type LaFeO$_3$ sensor, exposure to 5 ppm of CO gas at 250 °C leads to an injection of electrons into the valence band and their recombination with holes (generated in an oxygen ambient atmosphere), decreasing the concentration of holes and thereby increasing sensor resistance. After the CO is turned off, the sensing material starts to recover its path towards the initial resistance. The same trend was obtained for 3 and 1 ppm of CO at the same temperature but with a lower response. LaFeO$_3$ microspheres show a response of 17.1% for 5 ppm, 8.5% for 3 ppm and 4.5% for 1 ppm of CO. Fig. 13(b) shows the relative response plot of a sensor based on rGO-LaFeO$_3$ to various concentrations (5, 3 and 1 ppm) of CO at 200 °C where the responses are 30.9%, 15.5%, and 6.8%, respectively, indicating that the sensor thus fabricated can be used for CO detection with a wide range of smaller concentrations. The sensing mechanism is similar for rGO-LaFeO$_3$ to that for an LaFeO$_3$ sensor. As the temperature increases to 250 °C, the response is quite similar to that at 200 °C: *viz.* 31.9% for 5 ppm of CO, 17.7% for 3 ppm of CO and 8.8% for 1 ppm of CO. Fig. 13(c) represents the change in relative response with respect to concentration of test gases
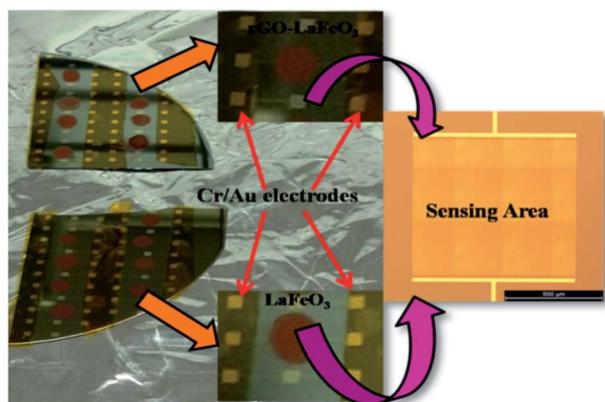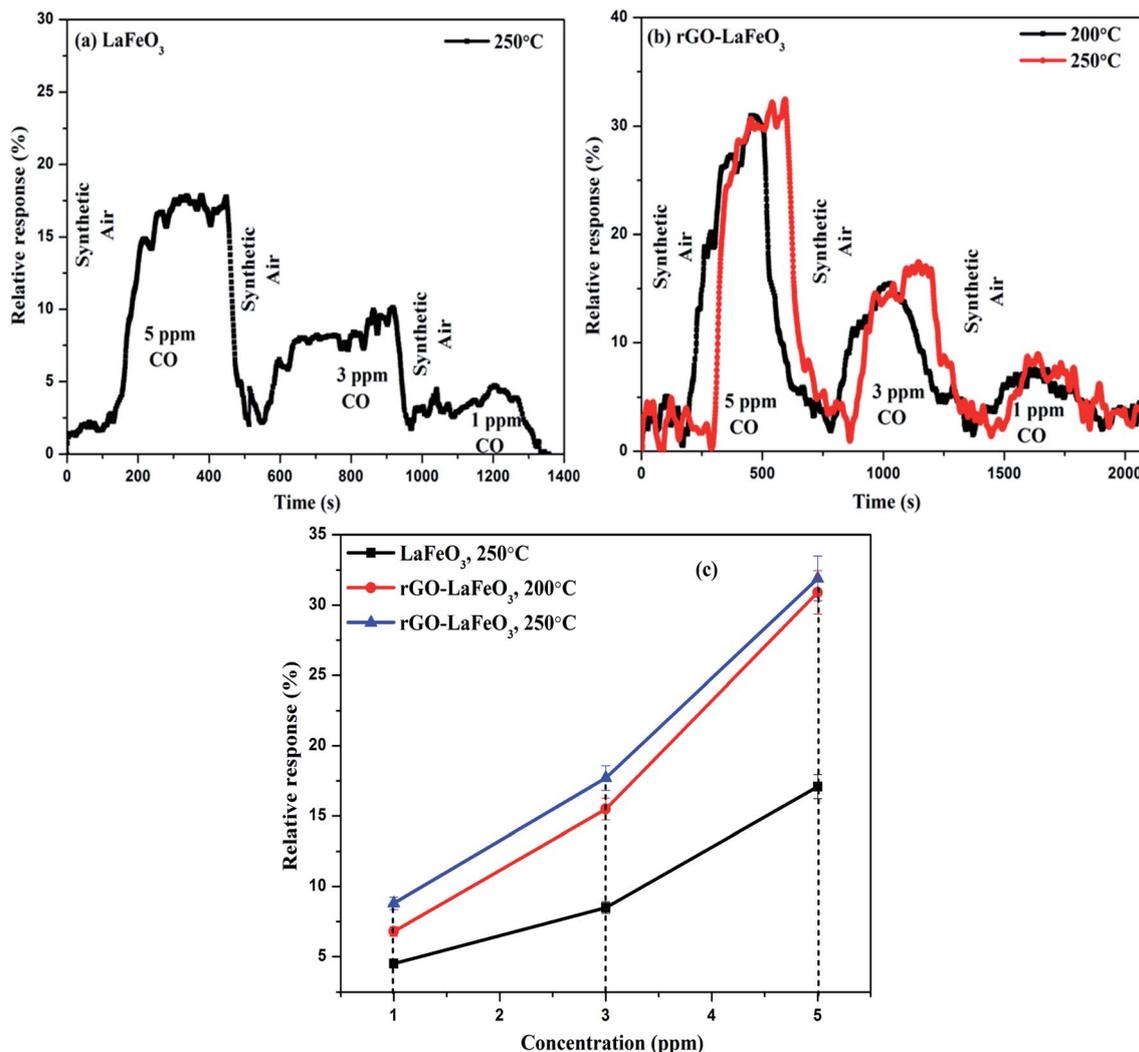
Fig. 13 Relative response with respect to time for LaFeO₃ (a) and rGO-LaFeO₃ (b) and relative response with respect to concentration for LaFeO₃ and rGO-LaFeO₃ (c) towards CO gas at temperatures of 200 and 250 °C.

for the fabricated sensors at temperatures of 200 and 250 °C. There is a clear and visible improvement in the sensing performance corresponding to the addition of carbon atoms through doping of reduced graphene oxide (rGO) into the LaFeO₃ which leads to an increase in the active sites and surface area for higher adsorption/desorption of gas molecules.

3.8.2 Nitrogen dioxide gas sensing. The gas sensing characteristics of LaFeO₃ and rGO-LaFeO₃ based sensors for 3, 2 and 1 ppm of NO₂ gas are shown in Fig. 14(a) and (b), respectively, at operating temperatures of 200 and 250 °C. Fig. 14(c) shows the relative response with respect to concentration for LaFeO₃ and rGO-LaFeO₃. LaFeO₃ does not show any response at all to concentration of NO₂ at 200 °C. However, at 250 °C, LaFeO₃ exhibits a high response. When 1 ppm of NO₂ is injected onto the surface of p-type LaFeO₃, it gives a 92.7% response and it reaches a higher value of 144.1 from 118.9 for an increase in concentration from 2 to 3 ppm. A sensor based on rGO-LaFeO₃

gave an even higher response at 200 °C upon exposure to NO₂: *viz.* 53.7%, 79.5% and 81.3% for 1 ppm, 2 ppm and 3 ppm, respectively. This relative response increased further for a temperature of 250 °C: *viz.* 129.9%, 159.9% and 183.4% for 1 ppm, 2 ppm and 3 ppm, respectively. The increase in response is due to the smaller band gap of rGO-LaFeO₃, which makes the flow of electrons/holes easier, to provide conductance. It is evident that the interactions of NO₂ with the LaFeO₃ surface are more complicated than those of CO. NO₂ can be absorbed on the surface of LaFeO₃ film in three different states: two nitrosyl types (NO⁻, NO⁺) and a nitro type (NO₂⁻).[26] The gas sensing mechanisms of LaFeO₃ with CO and NO₂ are described in ESI.† A comparison Table (S3)† of the gas sensing results for both samples with the already published literature is given in ESI,† and clearly indicates that rGO-LaFeO₃ gives a higher sensitivity than LaFeO₃ and is a potential material for gas sensing applications.
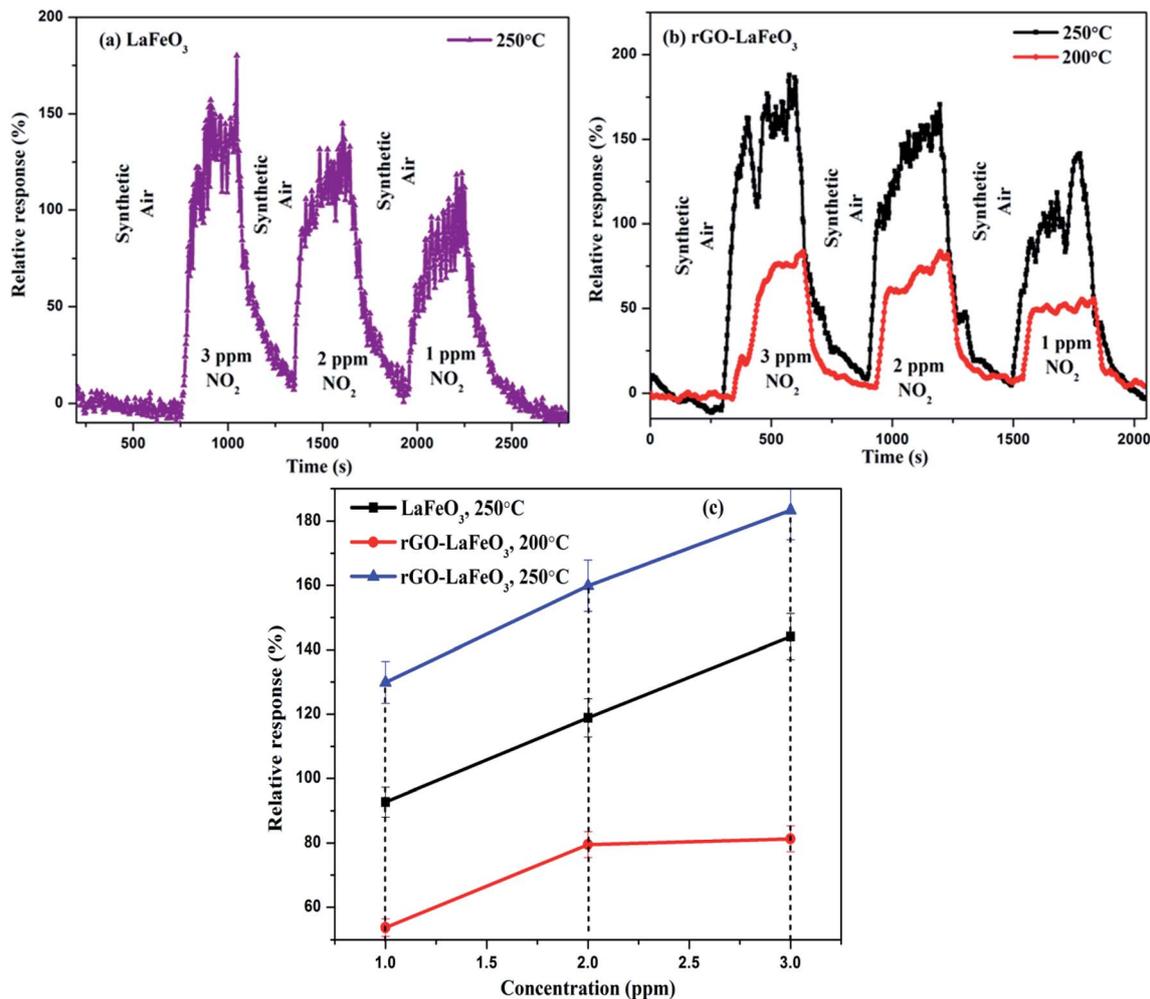
Fig. 14 Relative response with respect to time for LaFeO$_3$ (a) and rGO-LaFeO$_3$ (b) and relative response with respect to concentration for LaFeO$_3$ and rGO-LaFeO$_3$ (c) towards NO$_2$ gas at temperatures of 200 and 250 °C.

4. Conclusion

In summary, microspheres of LaFeO$_3$ and rGO-LaFeO$_3$ were synthesized by a hydrothermal method. Gas sensing devices (dimension 500 × 500 μm) using synthesized nanomaterials were successfully fabricated through photolithography using a drop cast method for film deposition. In terms of structure, morphology, thermal stability, and surface roughness, the samples show potential as gas sensing devices. An ortho-rhombic structure was observed for both products from X-ray diffraction. The appearance of a D′ band in the Raman spectra and an alkene/organic group in FT-IR confirm the formation of a composite. The synthesized products are thermally stable at a temperature of ∼720 °C. XPS and TEM confirm the presence of La, Fe, O, and C elements. Gas sensing measurements indicate that an rGO-LaFeO$_3$ based device exhibits a higher relative response than LaFeO$_3$ for both CO (5 ppm, 3 ppm, 1 ppm) and NO$_2$ (3 ppm, 2 ppm, 1 ppm) gases. It is also contributed that rGO-LaFeO$_3$ is highly selective for NO$_2$ gas even at 1 ppm concentration at 200 and 250 °C. This is mainly due to the higher surface area and smaller band gap of

rGO-LaFeO$_3$. To the best of our knowledge, this is the first study of an rGO-LaFeO$_3$ based gas sensing device with an excellent relative response.

Conflicts of interest

On behalf of all authors, the corresponding author states that there are no conflicts to declare.

References

1 S. Thirumalairajan, K. Girija, V. R. Mastelaro and N. Ponpandian, *ACS Appl. Mater. Interfaces*, 2014, **6**, 13917–13927.

2 P. Sun, W. Zhao, Y. Cao, Y. Guan, Y. Sun and G. Lu, *CrystEngComm*, 2011, **13**, 3718.

3 H. Wang, Y. Liu, M. Li, H. Huang, H. M. Xu, R. J. Hong and H. Shen, *Optoelectron. Adv. Mater., Rapid Commun.*, 2010, **4**, 1166–1169.

4 D. E. Motaung, G. H. Mhlongo, I. Kortidis, S. S. Nkosi, G. F. Malgas, B. W. Mwakikunga, S. S. Ray and G. Kiriakidis, *Appl. Surf. Sci.*, 2013, **279**, 142–149.

5 L. Gao, F. Ren, Z. Cheng, Y. Zhang, Q. Xiang and J. Xu, *CrystEngComm*, 2015, **17**, 3268–3276.

6 P. Su and S. Peng, *Talanta*, 2015, **132**, 398–405.

7 W. Yan, H. Fan, Y. Zhai, C. Yang, P. Ren and L. Huang, *Sens. Actuators, B*, 2011, **160**, 1372–1379.

8 R. Vyas, S. Sharma, P. Gupta, Y. K. Vijay, A. K. Prasad, A. K. Tyagi, K. Sachdev and S. K. Sharma, *J. Alloys Compd.*, 2013, **554**, 59–63.

9 R. Vyas, S. Sharma, S. Khan, R. Divakar, K. Sachdev and S. K. Sharma, *Macromol. Symp.*, 2015, **357**, 99–104.

10 R. Ghosh, A. Midya, S. Santra, S. K. Ray and P. K. Guha, *ACS Appl. Mater. Interfaces*, 2013, **5**, 7599–7603.

11 G. Lu, L. E. Ocola and J. Chen, *Appl. Phys. Lett.*, 2009, **94**, 8–11.

12 G. Lu, L. E. Ocola and J. Chen, *Nanotechnology*, 2009, **20**, 445502.

13 J. T. Robinson, F. K. Perkins, E. S. Snow, Z. Wei and P. E. Sheehan, *Nano Lett.*, 2008, **8**, 3137–3140.

14 J. D. Fowler, M. J. Allen, V. C. Tung, Y. Yang, R. B. Kaner and B. H. Weiller, *ACS Nano*, 2009, **3**, 301–306.

15 F. Yavari, Z. Chen, A. V. Thomas, W. Ren, H. M. Cheng and N. Koratkar, *Sci. Rep.*, 2011, **1**, 1–5.

16 A. Salehi-Khojin, D. Estrada, K. Y. Lin, M. H. Bae, F. Xiong, E. Pop and R. I. Masel, *Adv. Mater.*, 2012, **24**, 53–57.

17 S. Liu, J. Tian, L. Wang, H. Li, Y. Zhang and X. Sun, *Macromolecules*, 2010, **43**, 10078–10083.

18 M. Gautam and A. H. Jayatissa, *Mater. Sci. Eng., C*, 2011, **31**, 1405–1411.

19 N. Hu, Z. Yang, Y. Wang, L. Zhang and Y. Wang, *Nanotechnology*, 2014, **25**, 1–10.

20 C. Doroftei, P. D. Popa and F. Iacomi, *Sens. Actuators, B*, 2012, **161**, 977–981.

21 C. Doroftei and L. Leontie, *RSC Adv.*, 2017, **7**, 27863–27871.

22 E. Abdullah, A. Idris and A. Saparon, *ARPN J. Eng. Appl. Sci.*, 2017, **12**, 3218–3221.

23 N. Q. Minh, *J. Am. Ceram. Soc.*, 1993, **76**, 563–588.

24 S. Thirumalairajan, K. Girija, V. Ganesh, D. Mangalaraj, C. Viswanathan and N. Ponpandian, *Cryst. Growth Des.*, 2013, **13**, 291–302.

25 A. Benali, S. Azizi, M. Bejar, E. Dhahri and M. F. P. Graça, *Ceram. Int.*, 2014, **40**, 14367–14373.

26 N. N. Toan, S. Saukko and V. Lantto, *Phys. Rev. B: Condens. Matter Mater. Phys.*, 2003, **327**, 279–282.

27 J. W. Yoon, M. L. Grilli, E. Di Bartolomeo, R. Polini and E. Traversa, *Sens. Actuators, B*, 2001, **76**, 483–488.

28 B. A. I. Shouli, S. H. I. Bingjie, M. A. Lijing, Y. Pengcheng, L. I. U. Zhiyong, L. I. Dianqing and C. Aifan, *Sci. China, Ser. B: Chem.*, 2009, **52**, 2106–2113.

29 M. Cristina, G. Martinelli, Y. Sadaoka, P. Nunziante and E. Traversa, *Sens. Actuators, B*, 1998, **48**, 270–276.

30 X. Wang, H. Qin, L. Sun and J. Hu, *Sens. Actuators, B*, 2013, **188**, 965–971.

31 S. Nakayama, *J. Mater. Sci.*, 2001, **36**, 5643–5648.

32 M. Sorescu, T. Xu, J. D. Burnett and J. A. Aitken, *J. Mater. Sci.*, 2011, 6709–6717.

33 H. Xiao, C. Xue, P. Song, J. Li and Q. Wang, *Appl. Surf. Sci.*, 2015, **337**, 65–71.

34 N. Sharma, S. K. Sharma and K. Sachdev, *Ceram. Int.*, 2019, **45**, 7217–7225.

35 R. D. Kumar, R. Thangappan and R. Jayavel, *J. Inorg. Organomet. Polym. Mater.*, 2017, **27**, 892–900.

36 N. Sharma, V. Sharma, S. K. Sharma and K. Sachdev, *Mater. Lett.*, 2019, **236**, 444–447.

37 V. A. Online, S. Thirumalairajan, K. Girija, N. Y. Hebalkar, D. Mangalaraj, C. Viswanathan and N. Ponpandian, *RSC Adv.*, 2013, **3**, 7549–7561.

38 X. Ren, H. Yang, S. Gen, J. Zhou, T. Yang, X. Zhang, Z. Cheng and S. Sun, *Nanoscale*, 2016, **8**, 752–756.

39 F. Deganello, M. L. Tummino, C. Calabrese, M. L. Testa, P. Avetta, D. Fabbri, A. B. Prevot, E. Montoneri and G. Magnacca, *New J. Chem.*, 2015, **39**, 877–885.

40 J. Zhu, H. Li, L. Zhong, P. Xiao, X. Xu, X. Yang, Z. Zhao and J. Li, *ACS Catal.*, 2014, **4**, 2917–2940.

41 S. Acharya, D. K. Padhi and K. M. Parida, *Catal. Today*, 2017, 1–12.

42 K. M. Parida, K. H. Reddy, S. Martha, D. P. Das and N. Biswal, *Int. J. Hydrogen Energy*, 2010, **35**, 12161–12168.

43 S. Phokha, S. Pinitsoontorn, S. Maensiri and S. Rujirawat, *J. Sol-Gel Sci. Technol.*, 2014, **71**, 333–341.

44 B. Ding, C. Han, L. Zheng, J. Zhang, R. Wang and Z. Tang, *Sci. Rep.*, 2015, **5**, 1–10.

45 V. Di Castro and S. Ciampi, *Surf. Sci.*, 1995, **333**, 294–299.

46 *Preparation, characterization of perovskite LaFeO₃ nanospheres and its visible light*, 2013, ch. 4, pp. 65–81.

47 W. Weiss and W. Ranke, *Prog. Surf. Sci.*, 2002, **70**, 1–151.

48 K. Dave, K. H. Park and M. Dhayal, *RSC Adv.*, 2015, **5**, 95657–95665.

49 T. Anh, J. Sik, J. Su and Y. Tae, *Colloids Surf., A*, 2011, **384**, 543–548.

50 S. Liu, B. Yu, H. Zhang, T. Fei and T. Zhang, *Sens. Actuators, B*, 2014, **202**, 272–278.

51 P. Song, Q. Wang, Z. Zhang and Z. Yang, *Sens. Actuators, B*, 2010, **147**, 248–254.

52 J. Čejka and S. Mintova, *Cat. Rev.*, 2007, **4**, 457–509.